

IMPERIAL COLLEGE LONDON

DEPARTMENT OF AERONAUTICS

AERO97951

Applied Computational Aerodynamics Assignment 2

Group

Mr. Javier Leguina Peral
Mr. Fernando Acero Marchesotti

Supervisor

Prof. Joaquim Peiro

February 3, 2020

South Kensington Campus
Imperial College London
London SW7 2AZ
United Kingdom

1 Imperial College CFD Codes

PantaRhei is an interdisciplinary forecasting system for multi-scale flows, with significant contributions from Dr. Papadakis. It performs finite volume discretisations on fully unstructured grids. It is 2^{nd} order accurate in space and time for unstructured meshes, but up to 4^{th} order accurate in space for structured meshes, by making use of standard or limited central schemes. The turbulence model used is classical LES, that is Smagorinsky Subgrid Scale (SGS), which postulates a linear relationship between the shear stress and the resolved rate of strain tensor, i.e. the eddy viscosity assumption. This code is mainly used for global weather and climate forecasting, where the large hydrostatic scale and the small scale of the convective motions must be considered. It can also be used to model separated flow on an aerofoil with detailed leading edge and trailing edge vortex modeling.

pyFR is a python code developed by Dr. Vincent and others. It solves compressible Euler and Navier-Stokes equations, and the potential for any advection-diffusion type problem, although it is extremely focused on LES and DNS. It is based on high-order numerical methods for unstructured grids, the Flux Reconstruction (FR) approach. It can achieve any arbitrary spatial accuracy due to the FR approach. For FR schemes, the flux is continuous, but the solution may be discontinuous across cells. Riemann solvers are used for the flux, with a correction function applied to enforce flux continuity. For temporal accuracy, it incorporates multiple Runge-Kutta schemes. An advantage of FR methods is good spatio-temporal locality of the data. For this reason, the code has been developed to leverage the latest computational hardware developments, which present increase in FLOPS but no increase in memory access rates. These methods are able to combine the accuracy of high-order spectral methods or finite difference methods, while still allowing for the geometric flexibility of low-order finite volume or finite element methods. Regarding turbulence modeling, there is no explicit SGS model, but rather an implicit LES approach is used by making use of the inherent numerical dissipation of the FR approach at high frequencies. This code is particularly suitable for modeling unsteady turbulent flows such as channel flow with perturbations, separated flows or acoustic problems, with modern hardware.

Incompact3D is a high-order finite-difference flow solver by Dr. Laizet dedicated to solving turbulent incompressible flow. For this, the Poisson equation is modelled over the spectral space due to its efficiency. It is based on a 6^{th} order finite difference discretisation of the incompressible Navier-Stokes equations over a Cartesian grid. To correctly model complex geometries with this mesh, it introduces a forcing function ϵ to the Navier-Stokes equations, which emulates a 0 velocity condition within solids. However, the Cartesian mesh curved surfaces are not well mapped. This also introduces velocity discontinuities. To solve it, it improves the immersive boundary method by removing the discontinuity, locating the wall accurately, thus modeling the shape exactly. Hence, a high number of mesh points are needed, which requires parallelisation techniques. The scalability of this approach has been proven to be of up to 1×10^6 cores. It uses either Runge-Kutta or Adam-Bashford schemes for time advancements. It is dedicated to performing DNS and LES. For low Reynolds, this scheme does not use turbulence models as it is directly solving Navier-Stokes equations, but to reach realistic Reynolds numbers, an implicit Large Eddy Simulation strategy can be used. This code finds its best application for the resolution of low Reynolds phenomena at all fluid scales to improve our understanding transfer of energy between scales.

Nektar++ is a high-order spectral/hp method developed by Prof. Sherwin and Dr. Cantwell amongst others. As a spectral/hp method, it is a finite element method that is able to combine low polynomial order h-type solvers as well as higher p-order piecewise polynomial order solvers. It can solve 1-, 2- or 3-D problems. It implements both continuous and discontinuous Galerkin solvers, as well as FR operators. For turbulence modeling, it implements a Spectral Vanishing Viscosity approach, which is viewed as an alternative iLES approach. The code also allows for time integration of Navier-Stokes to perform DNS. It also supports linearised and adjoint forms of Navier-Stokes. It finds applications in many aerodynamics such as turbine blade flow modeling or car aerodynamics, as well as biomedical engineering problems such as biological flow modeling. It is for use mainly with incompressible flow although it can solve compressible flow too. It can solve any reaction-diffusion-advection problem.

2 STAR-CCM+ Aerofoil Simulations

2.1 Individual Task (a) by Fernando Acero Marchesotti

The boundary layer thickness can be estimated from the turbulent Blasius solution over a flat plate, given by

$$\delta \approx 0.37x/\text{Re}_x^{1/5} \quad (1)$$

where $\text{Re}_x = \rho u x / \mu$ is the Reynolds number based on root chord characteristic length x , and all other variables take free-stream values. For the flow parameters in Table 1, $\delta \approx 0.02335$ m.

The wall friction coefficient for a turbulent boundary layer can be estimated from Prandtl's one seventh power law,

$$c_f = \frac{0.0027}{(\text{Re}_x/x)^{1/7}} \Rightarrow \tau|_{\text{wall}} = 1/2 \rho u^2 c_f \Rightarrow u|_{\text{wall}} = \sqrt{\frac{\tau|_{\text{wall}}}{\rho}} \quad (2)$$

where $\tau|_{\text{wall}}$ is the wall shear stress and the wall velocity $u|_{\text{wall}}$ is obtained from dimensional analysis. The wall element thickness Δs is given by

$$\Delta y|_{\text{wall}} = \frac{y^+ \nu}{u|_{\text{wall}}} \Rightarrow \Delta s|_{\text{wall}} = 2\Delta y|_{\text{wall}} \quad (3)$$

where $y^+ = 1$ and the element thickness Δs is twice the value of Δy because cell values are taken at the centroid of the cell. Based on the given flow parameters, the estimate for the wall element thickness is $\Delta s = 4.39 \cdot 10^{-5}$ m.

The thickness of the elements along the prism layer follows the geometric series

$$l_n = l_1 r^{n-1} \Rightarrow l_{\text{tot}} = \sum_{k=1}^n l_1 r^{k-1} = \frac{l_1 (r^n - 1)}{r - 1} \quad (r \neq 1) \quad (4)$$

where l_{tot} is the total thickness of the prism layer, n is the number of elements in the prism layer and r is the growth rate of the layer. In our case, since the growth factor of the domain is 1.15, a good approach to for selecting the number of prism layers is to chose one such that the growth rate of the prism layer is greater or equal to 1.15. Using Equation 4, the number of prism layers was chosen to be $n = 43$.

Table 1: Far flow field parameters.

Re [-]	M [-]	x [m]	p [Pa]	ρ [kg/m ³]	T [K]	α [°]	γ [-]	a [m/s]	u [m/s]	μ [Pa s]	ν [m ² /s]
300000	0.3	1	101325	1.225	288.15	6	1.4	340.29	102.09	$1.25 \cdot 10^{-4}$	$1.02 \cdot 10^{-4}$

The force coefficients obtained for varying domain radii are presented in Figure 1a. It can be seen that as the domain radius is increased, C_l and C_d values tend to converge. Figure 1a shows that it is more complicated to obtain a converged value for C_d . As the domain radius was increased, the drag that corresponds to pressure forces (i.e. induced drag) increased whereas the drag caused by shear forces on the aerofoil's surface (i.e. skin-friction drag) did not present considerable changes. This is due to the difficulty to model the wake appropriately for small domain radii. For the following investigations, a domain radius of 50 m is chosen as it provides sufficiently accurate force coefficients when compared to reference values taken at 100 m, as shown in Table 2, while still providing computational savings. The chosen point can be found in Figure 1 marked with a black circle.

Following the decision to fix the radius at 50 m, an investigation in the effect of base size was performed. The results are presented in Figure 1b. For base sizes above 0.01 m, the prism layer thickness was increased to values given by Equation 4 such that the growth rate between the prism

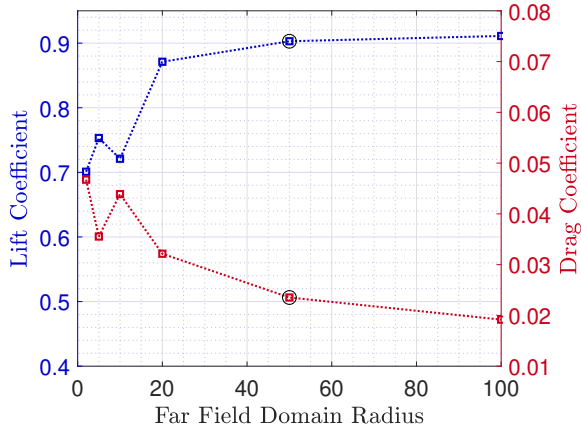
Table 2: Values of lift and drag coefficient for the chosen points and relative difference to the reference point.

Base size	R_{domain} [m]	C_l	C_d
0.01	100	0.91105	0.01917
0.01	50	0.9029	0.0235
0.005	50	0.91463	0.01896

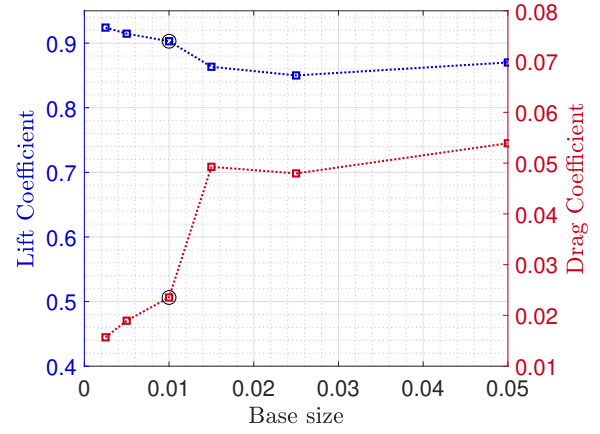
mesh and the polygonal mesh were consistent. For base sizes below 0.01 m, the prism layer thickness was not reduced as this would have implied a layer thickness smaller than the boundary layer thickness estimate provided by Equation 1, leading to inaccurate modeling of the boundary layer.

As expected, results of Figure 1b present convergence as the base size is reduced, whereas divergence in the results was observed for base sizes larger than 0.01 m (particularly for the drag coefficient). The pressure distribution for varying base sizes is shown in Figure 2, where it can be seen how large base sizes fail to capture the suction peak at the leading edge. Moreover, it was found that for a base size of 0.005 m and domain radius 50 m, the force coefficients presented excellent agreement with the reference values taken in the domain radii investigation (base size 0.01 m and radius 50 m), as it can be seen in Table 2. A base size of 0.0025 m does not provide significant accuracy; it can be seen in Figure 2 how the pressure distribution overlaps with that for base size 0.005 m. This indicates that a base size of 0.005 m should be selected for further simulations.

Furthermore, a base size of 0.005 m provides a sufficiently smooth mesh of the aerofoil surface, as shown in Figure 3. It is the smallest base size for which the leading edge is not modelled as an sharp angle, but rather is modelled as a relatively curved surface as shown in Figure 3a. Similarly, as shown in Figure 3b, the base size is small enough such that for the chosen prism layer parameters, the mesh around the trailing edge is sufficiently smooth, which should help with the modeling of the wake.



(a) Lift and drag coefficients for varying far field domain radii.



(b) Lift and drag coefficients for varying domain Base size.

Figure 1: Lift and drag coefficients for varying domain radius and Base size. The black circled point represents the same parameters in both Figures.

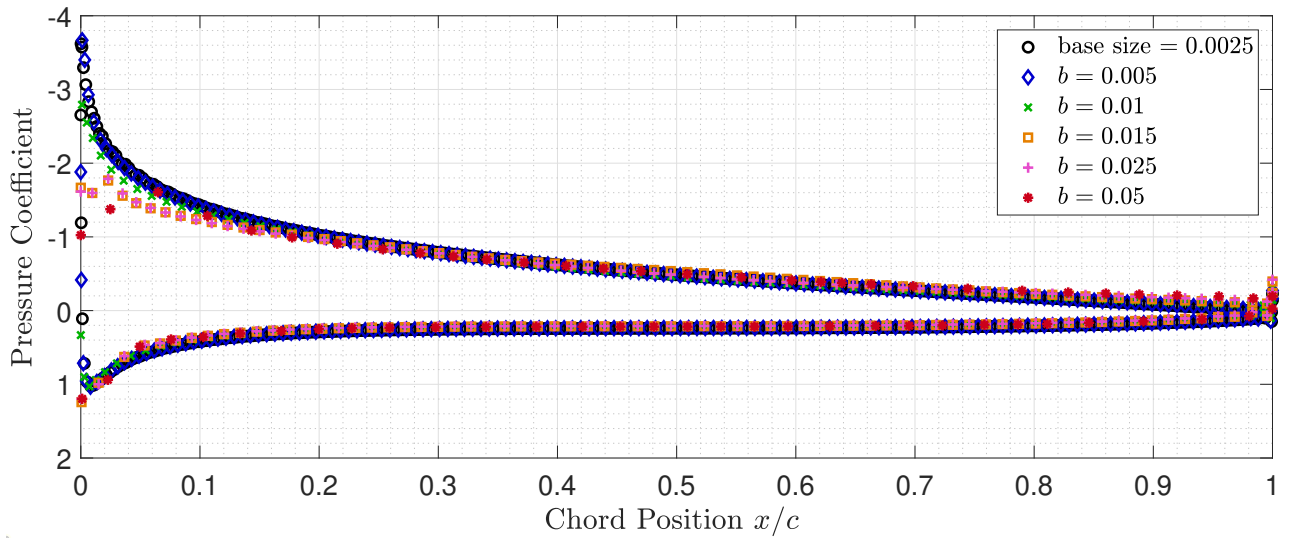


Figure 2: Pressure coefficients for varying domain Base size.

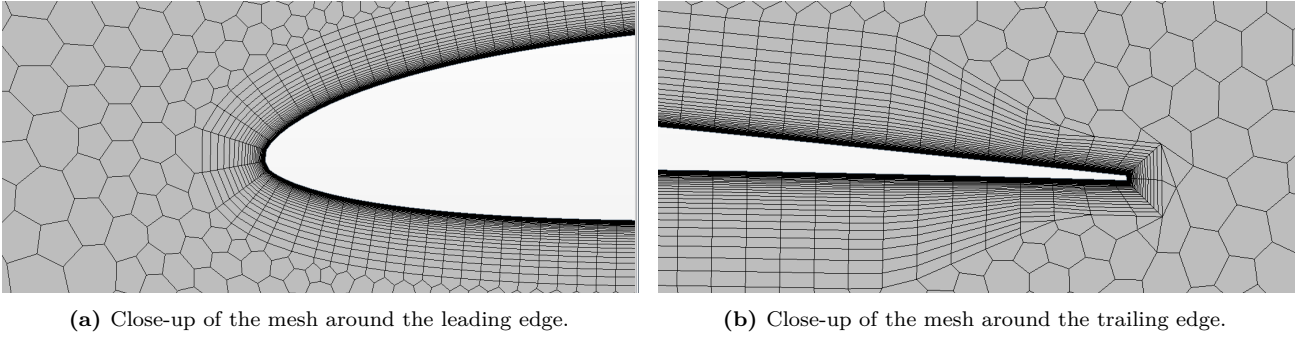


Figure 3: Close-up views of the mesh near the leading and trailing edges.

2.2 Individual Task (b) by Javier Leguina Peral

In order to increase the working efficiency while comparing different angles of attack, a series of global parameters were defined under **Tools > Parameters**. These values were the total velocity of the flow (**Speed** = 102.9 m/s) and the angle of attack (**AoA**). These were later called to initialise the flow direction \vec{d} and far field free flow boundary conditions \vec{V} as:

$$\vec{d} = [\cos(\text{\texttt{\$AoA}}), \sin(\text{\texttt{\$AoA}}), 0.0],$$

$$\vec{V} = [\text{\texttt{\$Speed}} \times \cos(\text{\texttt{\$AoA}}), \text{\texttt{\$Speed}} \times \sin(\text{\texttt{\$AoA}}), 0.0].$$

In this sense, the lift and drag coefficients obtained for the different settings can be seen in Table 3. These values were found after the following asymptotic stopping criterion was applied in STAR-CCM+ for the force coefficients: the last 20 samples for the C_l and C_d had to be within a range of 1×10^{-4} and 1×10^{-6} respectively.

Table 3: Values for the lift coefficient C_l and drag coefficient C_d found for various angles of attack.

	$\alpha = 0^\circ$	$\alpha = 2^\circ$	$\alpha = 4^\circ$	$\alpha = 6^\circ$	$\alpha = 8^\circ$	$\alpha = 10^\circ$
C_l	0.25520	0.46822	0.69558	0.91495	1.10739	0.83876
C_d	0.00991	0.01050	0.01196	0.01505	0.02263	0.08769

Figures 4a and 4b show the iteration history of the residual magnitudes and force coefficients until convergence at an angle of attack of 4° . This occurred after 817 iterations.

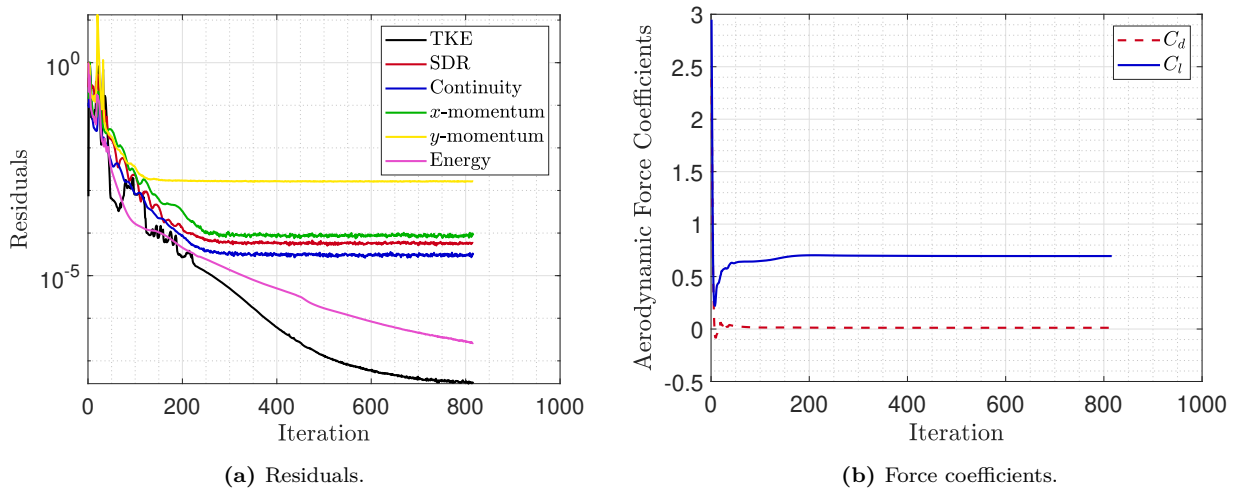


Figure 4: Iteration history for various quantities at angle of attack of 4° .

The flow was also simulated for an angle of attack of 10° . As it can be seen from Table 3, there is a significant drop in the C_l with a fourfold increase in C_d . From this, it is clear that the flow is separated. This was also clear in the velocity field of the flow throughout the simulation.

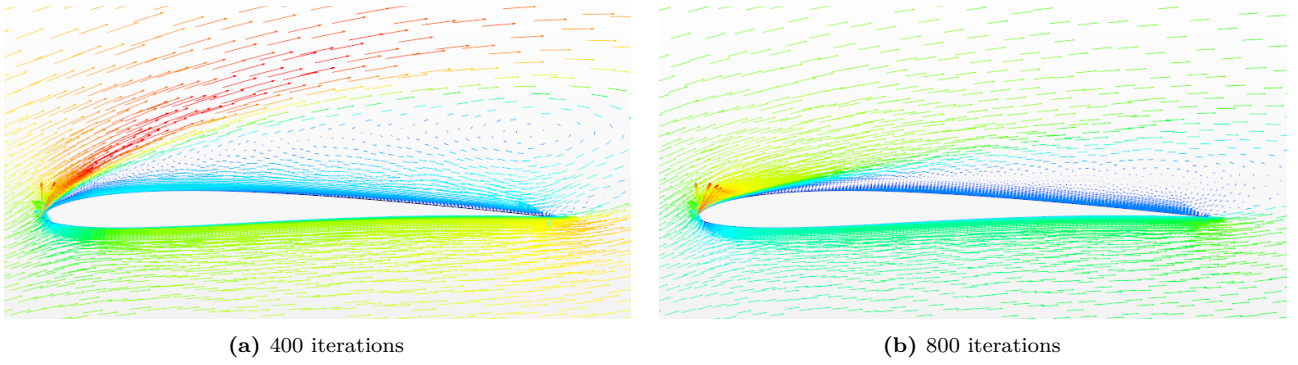


Figure 5: Velocity field throughout the simulation for an angle of attack of 10° .

As it can be seen in Figure 5a, the flow is separated from very early chordwise. As the simulation progresses, a region near the leading edge reattaches. However, in the the separated regions in both images a large region of vorticity is present. In fact, Figure 5b displays a weak von Kármán vortex street. These unstable phenomena also impact other relevant magnitudes of the computation such as the residuals and the aerodynamic forces.

Indeed, Figure 7 shows a pattern of oscillations in the residual magnitudes which hinders convergence to a stable flow condition. This can be understood as a consequence of the flow unsteadiness generated by the separation and the respective vorticity.

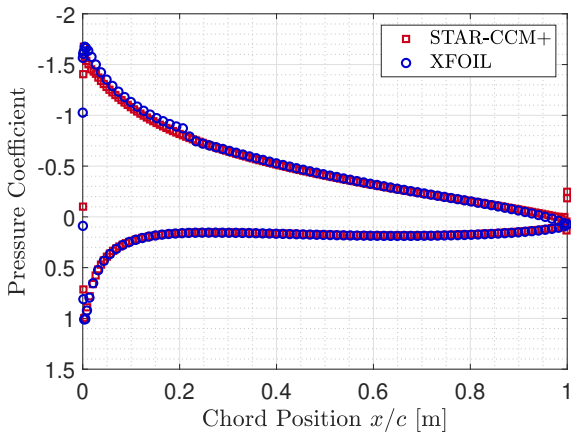


Figure 6: Comparison of C_p values for STAR-CCM+ and XFOIL for an angle of attack of 4° .

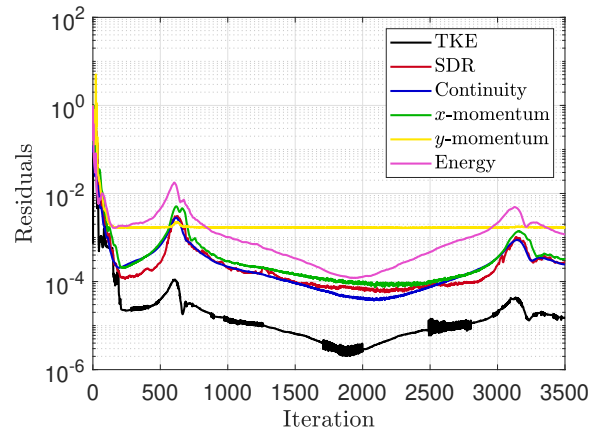


Figure 7: Residual magnitudes at an angle of attack of 10° .

Finally, the values of the pressure coefficient obtained for an angle of attack of 4° were plotted together with the results from a viscous simulation in XFOIL for the same incidence. This is shown in Figure 6. There are two remarkable features in this plot that deviate from the uniformity of results.

First, a clear increase in C_p values for the XFOIL simulation can be noted. The most probable reason for this phenomenon is the fact that the aforementioned simulation was run under a free transition model, as opposed to a fully-turbulent boundary layer in the STAR-CCM+ simulation. Given that a laminar boundary layer incurs in less losses as compared to a turbulent one, it can be concluded that the XFOIL simulation has a laminar boundary layer until transition at approximately $x/c = 0.2$. From this point on, C_p values remain very close in both simulations. This occurs albeit XFOIL having a viscous regime only in the boundary layer, but not in the free flow. This suggest the accuracy of the boundary layer thickness calculation in the XFOIL calculation is of extreme importance.

Second, the STAR-CCM+ simulation gives different results that the XFOIL simulation as it approaches the trailing edge. This is because the STAR-CCM+ model has a cropped trailing edge as a result of the geometry import. This feature generates a region of low pressure at the back of the wing, which explains the lower-than-expected C_p .

2.3 Joint Task (c)

The force coefficients obtained from XFOIL and STAR-CCM+ are presented in Figure 8. The fact that the same mesh was used for multiple angles of incidence is not ideal, as the flow need not be resolved to the same level of detail at every location around the aerofoil. For instance the presence of a stronger wake -and eventually a very early separation for high angles of attack- should lead to a mesh tailored to resolve these. Therefore, higher angles of attack would benefit from greater mesh resolution near the leading and trailing edges.

Moreover, the results presented in Figure 8 show that there is good agreement for both force coefficients except for high angles of attack.

Regarding the drag coefficient, XFOIL underestimates its magnitude as compared to STAR-CCM+. This is hypothesized to be because, given that XFOIL has a free-transition model, skin friction during the laminar phase will be lower than that of STAR-CCM+, which has a fully turbulent boundary layer. Divergence might also arise due to factors such as the choice of turbulence amplification factor or the boundary layer thickness. This is especially relevant given that XFOIL assumes the flow outside of the boundary layer to be inviscid. Thus, if the boundary layer thickness is not appropriate, relevant viscous effects will be neglected.

For the lift coefficient, there are only slight discrepancies. This might have to do with the fact that for lift, to obtain the total velocity at each point on the wake of the aerofoil given an angle of attack, “the wake trajectory is taken from an inviscid solution at that alpha” (Prof. Drela, XFOIL Manual). Hence, viscous effects that should decrease lift and increase drag from the wake are not considered. This is most prominent on or around stall, also due to the assumption of steady flow, which neglects the effects of the vortex street generated by the separated flow.

In fact, at an angle of incidence of 10° , the divergence in results is considerable. As it has been said XFOIL is known to present limitations in predicting flow separation that occurs at high angles of attack, due to the fact that it uses a viscous solver for the boundary layer only, with an inviscid solver for the rest of the flow field. Alternatively, STAR-CCM+ is using a fully viscous model across all the flow field, therefore separation will be predicted much more accurately. Since separation is characterised by viscous turbulent flow, STAR-CCM+ C_d data will be more accurate than XFOIL.

Regarding the values of y^+ for the different simulations, it can be seen in Table 4 that these never exceed the target value. Therefore, the k- ω SST turbulence model is solved appropriately and the boundary layer is correctly modeled.

Finally, regarding the physics models, those used for the STAR-CCM+ are preferred than those of XFOIL. Nevertheless, there are two major caveats with this particular simulation. Firstly, the fully turbulent boundary layer modeling may lead to inaccurate results for low angles of attack, where there should be a laminar boundary layer throughout the first section of the aerofoil (although Re is high enough for this to not be too significant). Secondly, the steady flow assumption should be appropriate for most angles of attack except for high enough angles such that separation occurs and unsteady behaviours are expected.

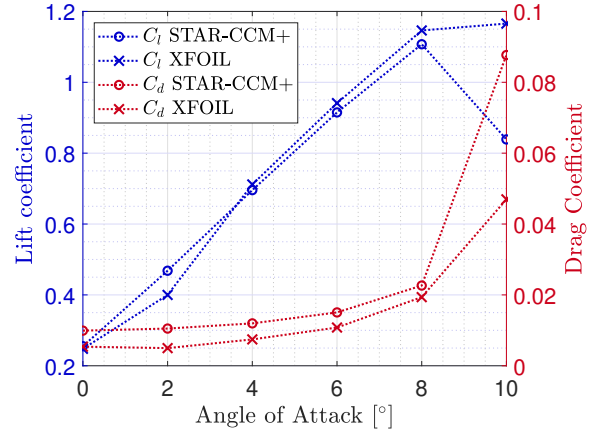


Figure 8: STAR-CCM+ and XFOIL lift and drag coefficients estimates for an angle of attack range of $\alpha \in [0^\circ, 10^\circ]$.

Table 4: Maximum y^+ values for different angles of attack.

α	y_{max}^+
0°	0.40571
2°	0.46493
4°	0.64403
6°	0.72726
8°	0.80313
10°	0.73367

3 STAR-CCM+ Wing Simulations

3.1 Individual Task (a) by Javier Leguina Peral

The meshes generated for the inviscid simulations of the wing can be seen in Figures 13a and 13b. After all the prescribed parameters were set, it was decided not to use a prism layer for this case. Recall that the need of a prism layer arises as a consequence of trying to capture the behaviour of the

boundary layer throughout its various regions as according to the Law of the Wall (see von Kármán, “Mechanical Similitude and Turbulence”, 1930). In this context, the requirement that $y^+ < 1$ for the first element of the prism layer is not relevant. Thus, the only free variable left was the base size.

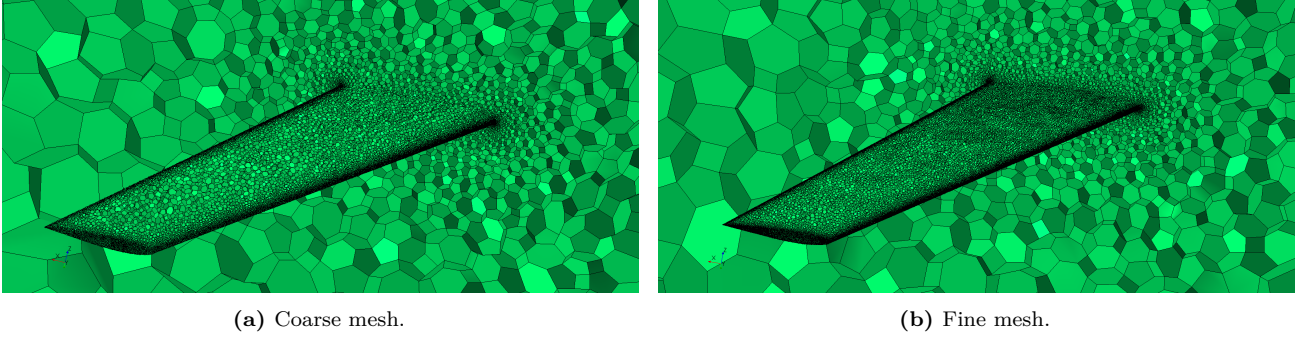


Figure 9: Scenes of the meshes generated for the inviscid simulation.

To generate meshes within the range given for the number of cells, the base size was chosen to be: 0.00634 m for the coarse mesh, yielding 310334 cells; and 0.00325 m for the fine mesh, resulting in 615779 cells.

The appropriate values for the flow speed, temperature and pressure were obtained assuming the desired Mach number and Reynolds number for each case were consistent with the ISA atmospheric model. By iterating values for the flow velocity and assumed operating altitude according to Algorithm 1 were obtained. Interpolating on a standard atmospheric model resulted in the values from Table 5. Note that the tolerance limit of 0.2% was deemed appropriate for a suitable equilibrium between precision and computational cost.

The convergence history of the aerodynamic force coefficients for the inviscid simulations can be seen in Figures 10b and 10b. Once converged, the obtained values for these magnitudes can be seen in Table 6. Moreover, the residual magnitude convergence for the case of a fine mesh at a Mach number of $M = 0.8$ can be seen in Figure 10c.

Table 5: Operating conditions.

	Altitude [m]	U [m/s]	T [°K]	P [Pa]	ρ [kg/m ³]
$M = 0.4$	3742.50	130	263.82	63737.02	0.8416
$M = 0.8$	10295.00	239	221.23	25263.96	0.3978

Algorithm 1 MATLAB code for flight conditions

Result: Operating velocity U_f and altitude H_f
 Initialise γ , chord, Re_f , M_f ;
for $U \in [0, 1000]$ **do**
 for $H \in [0, 15000]$ **do**
 $T, a, P, \rho \leftarrow \text{atmosisa}(H)$;
 $\mu \leftarrow \text{Sutherland's Law}$;
 $Re \leftarrow \rho U c / \mu$; $M \leftarrow U/a$;
if $Re - Re_f < 0.2\% \ \& \ M - M_f < 0.2\%$ **then**
 $U_f \leftarrow U$; $H_f \leftarrow H$;
end
end
end

Table 6: Force coefficients for the inviscid case.

	Coarse		Fine	
	$M = 0.4$	$M = 0.8$	$M = 0.4$	$M = 0.8$
C_L	0.15706	0.20393	0.15692	0.20439
C_D	0.00239	0.00619	0.00202	0.00558

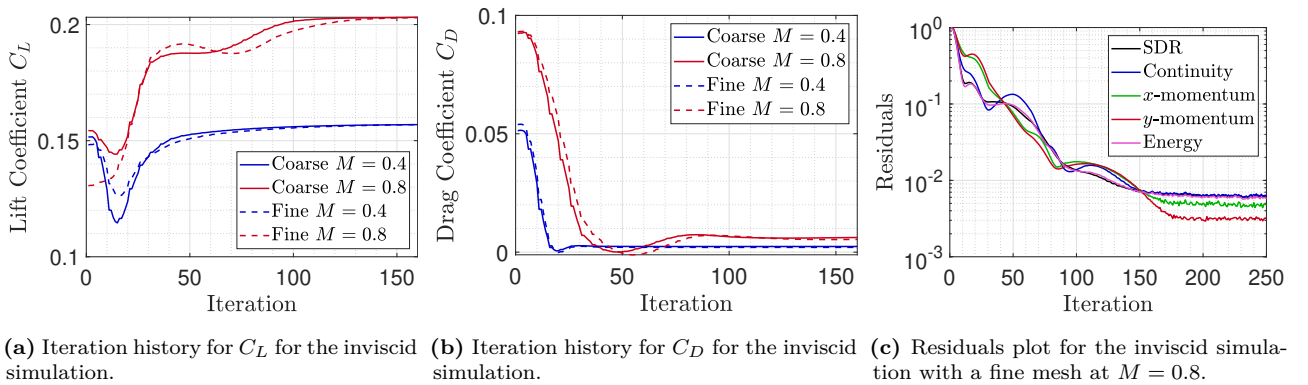


Figure 10: Iteration history for various magnitudes at an angle of attack of 2° .

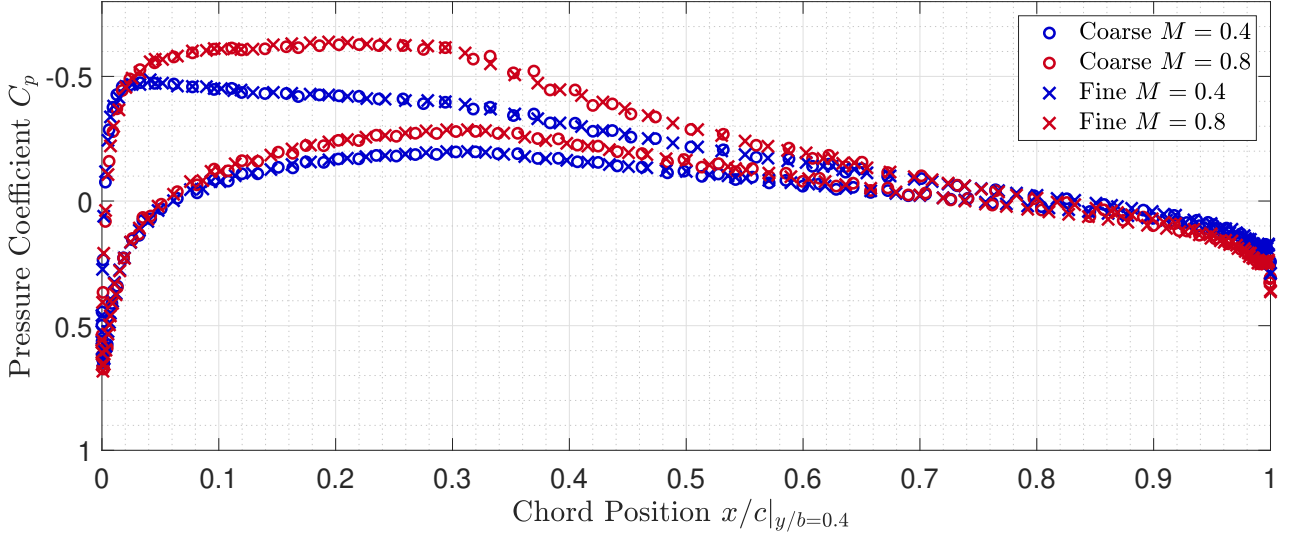


Figure 11: Pressure coefficient C_p for the inviscid simulation near mid-wing.

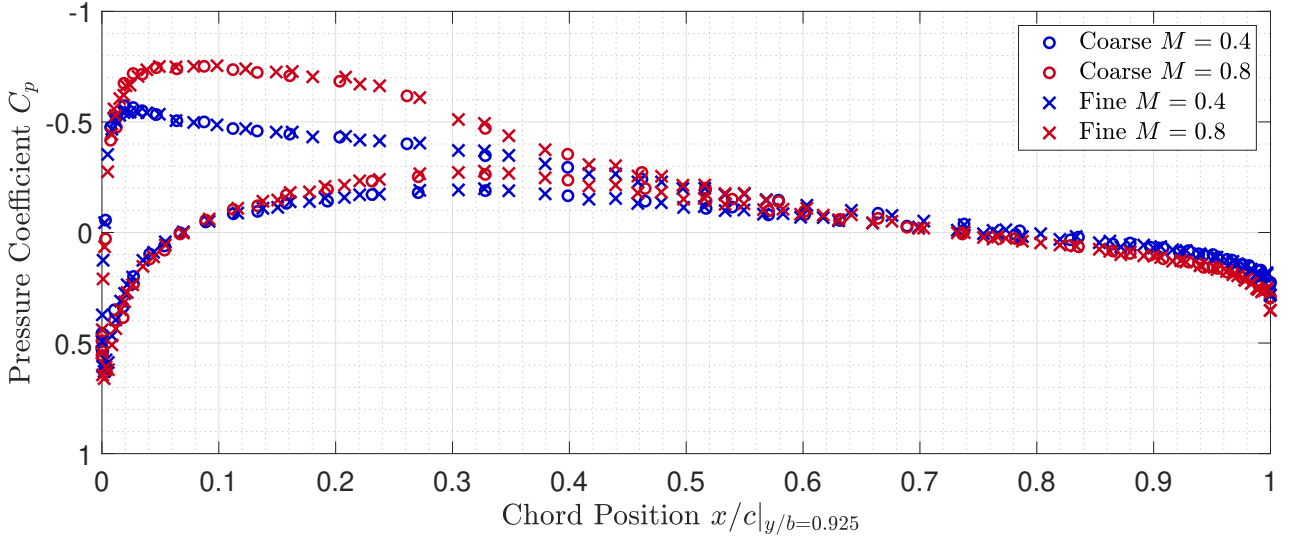


Figure 12: Pressure coefficient C_p for the inviscid simulation near the wing-tip.

3.2 Individual Task (b) by Fernando Acero Marchesotti

The boundary layer thickness was estimated using Equation 1, yielding $\delta \approx 0.00356$ m. A fine and a coarse mesh were created to follow the target cell numbers. An initial guess for the wall element thickness was given by Equation 3, yielding $\Delta s = 7.04 \times 10^{-6}$ m. A iterative search for the base size that would give the target total cell numbers was performed for each mesh. Due to the requirement for $y^+ < 1$ together with the total cell number requirements, the wall element thickness had to be reduced to 1×10^{-7} m. The number of prism layers was chosen following a similar heuristic described in 2.1, in order to present a smooth growth factor transition. The parameters used for generating each mesh are presented in Table 8, including the final number of cells for each mesh.

The flow parameters were set following the methods described in 3.1, i.e. an atmospheric fitting for pressure, temperature and density variations with altitude and Sutherland's law for viscosity. The values are shown in Table 5.

The iteration history of the lift and drag coefficients for all viscous simulations can be found in Figures 14a and 14b respectively, showing convergence for all simulations. The iteration history of the residuals for the viscous simulation with the fine mesh at $M = 0.8$ is presented in Figure 14c, which further confirms the convergence of

Table 7: Values for the force coefficients for various meshes and Mach numbers for the viscous simulations.

	Coarse		Fine	
	$M = 0.4$	$M = 0.8$	$M = 0.4$	$M = 0.8$
C_L	0.15225	0.19753	0.15025	0.19646
C_D	0.01530	0.02924	0.01366	0.02633

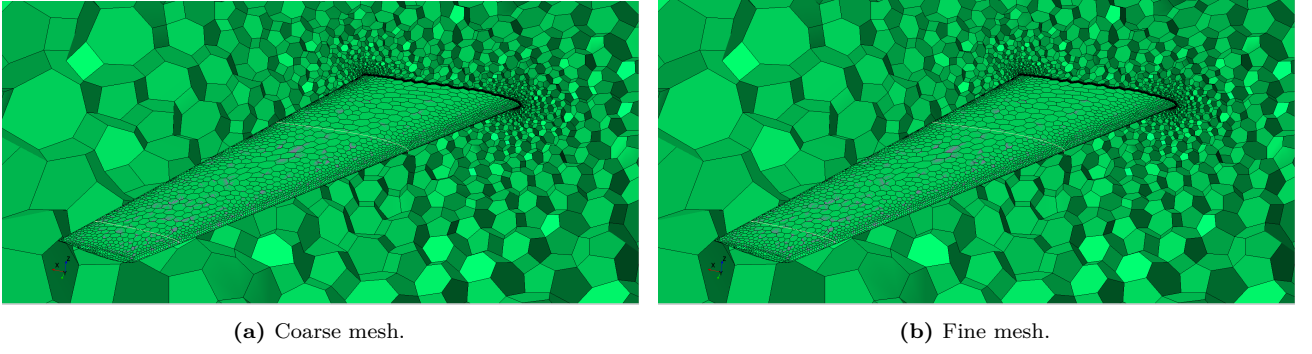


Figure 13: Scenes of the meshes generated for the viscous simulation.

the results. The converged results for all simulations are presented in Table 7.

Mesh	Total Prism Layer Thickness [m]	Near Wall Layer Thickness [m]	Number of Prism Layers	Base Size [m]	Number of Cells
Coarse	0.0036	1×10^{-7}	40	0.02	307954 [+2.65%]
Fine	0.0036	1×10^{-7}	40	0.012	589943 [-1.68%]

Table 8: Mesh parameters for coarse and fine meshes. Number of cells compared to targets in brackets.

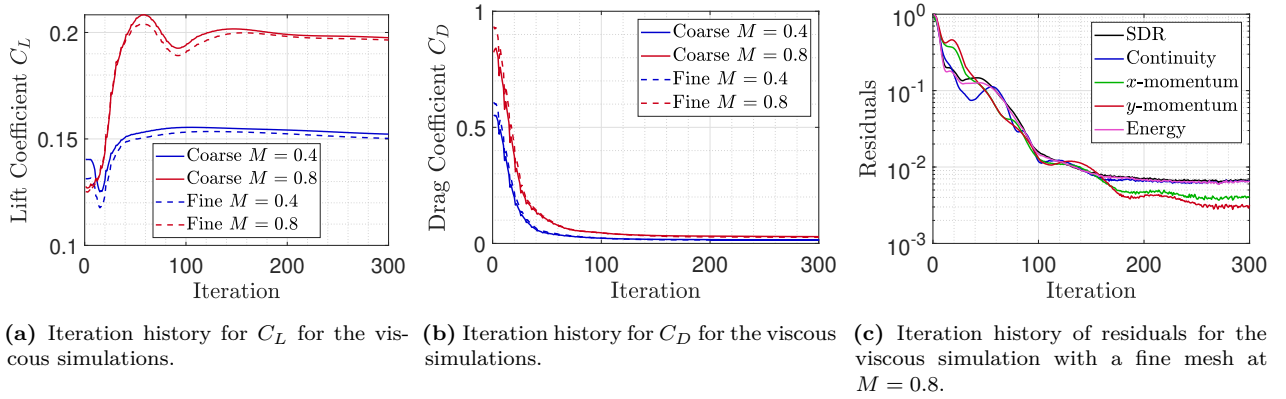


Figure 14: Iteration history for various magnitudes at an angle of attack of 2° .

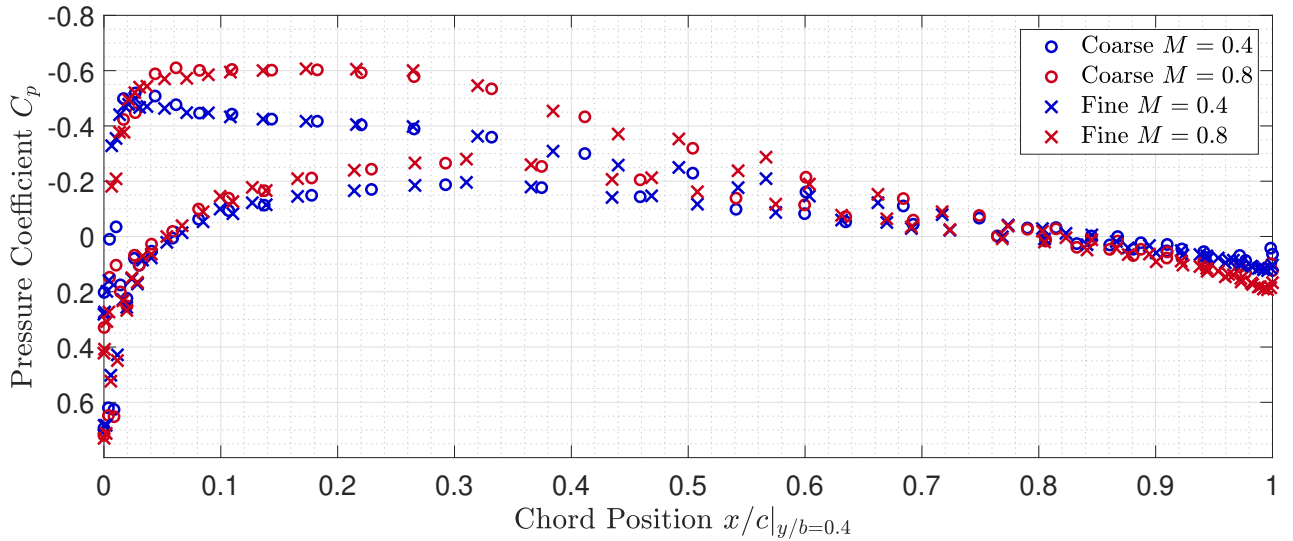


Figure 15: Pressure coefficient C_p for the viscous simulation near mid-wing.

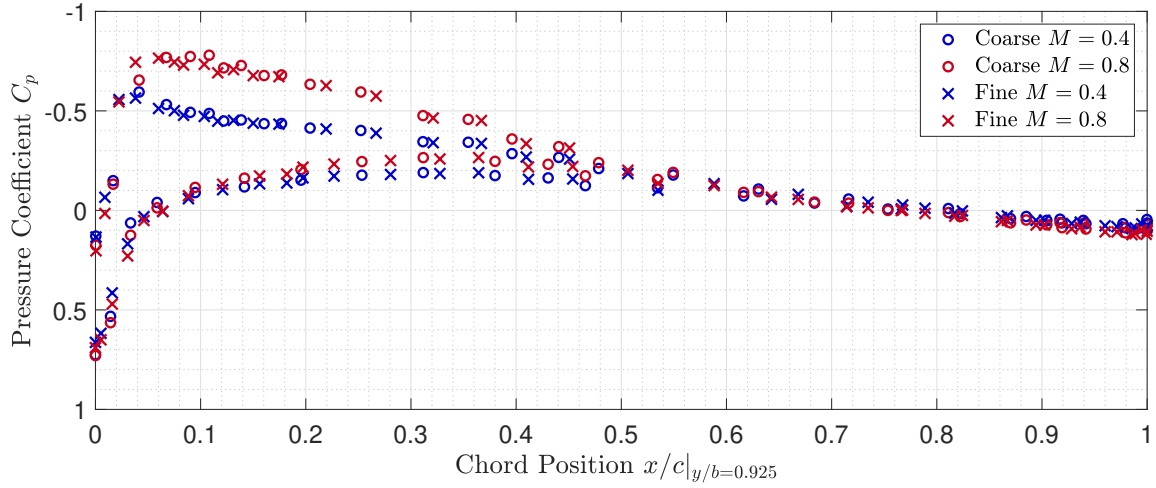


Figure 16: Pressure coefficient C_p for the viscous simulation near the wing-tip.

3.3 Joint Task (c)

The coarse mesh does not capture the shock properly, whereas fine mesh can. This is because for the transonic flow regimes, the changes in flow velocity that lead to a shock wave being formed occur over a short x/c length (region near the leading edge). A mesh that is too coarse will tend to smear the velocity gradients present on the aerofoil's top surface. This could be seen in the higher smoothness of the finer mesh scalar field as opposed to that of the coarse mesh (Figure 17).

Pressure distributions for the fine meshes at $M = 0.8$ are found in Figure 19 and 20, showing good agreement with experimental data at $y/b = 0.925$ but slight differences at $y/b = 0.4$, especially around the supersonic flow region ($C_p < C_p^{crit} = -0.43$). This is most likely due to the smearing of the shock in the simulation due to numerical and mesh limitations.

For the inviscid flow simulations, there are no requirements for the prism layer as there is no boundary layer, as explained in section 3.1. For the viscous simulations, there are three main requirements such that the prism layer correctly models the boundary layer. Firstly, the total thickness of the prism layer must be greater or equal to the estimated thickness (Blasius flat plate solution used here). Secondly, the wall element thickness must be able to capture the viscous sublayer –as defined by the Law of the Wall ($y^+ < 5$)– consistently with the turbulence solver used. This implies that $y^+ < 1$ for the first element (although it may be extended to $y^+ < 5$ with some loss of accuracy). Thirdly, the growth factor of the prism layer must lead to a sufficiently smooth transition between the prism layer and the polygonal mesh. Here, the polygonal mesh growth factor was left to the default 1.3, therefore the number of prism layers had to be chosen such that the growth factor of the prism layer was greater or equal to 1.3 (in our case prism layer followed geometric series as explained above, but it could have also followed a hyperbolic distribution).

The aforementioned requirements do not place conditions on base size, which ultimately determines the width of the wall elements in the prism layer. Nevertheless, this does affect the value of y^+ for a given wall element thickness: a too small base size will lead to an increase computational load as it also affects the far field mesh. Therefore, in order to achieve the target y^+ , a trade-off between base size and wall element thickness had to be found iteratively.

Regarding the variation of entropy near the wall for the inviscid case, it can be shown that, since the flow domain has been modelled as an adiabatic system with a constant temperature for the domain boundary at the far field, the entropy production is given by Equation 5. This implies

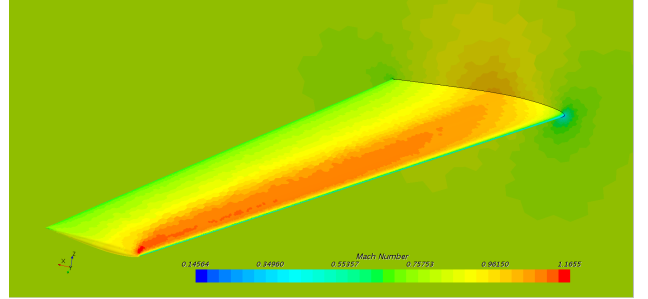


Figure 17: Mach number scalar field for the inviscid simulation with a coarse mesh at $M_\infty = 0.8$.

$$\nabla s = -\frac{h}{T} \frac{\nabla \rho}{\rho} - \frac{\vec{v} \times (\nabla \times [\rho \vec{v}])}{\rho T} \quad (5)$$

that, although velocity gradients will not be generated due to the shear forces otherwise involved near the wall, entropy generation will occur due to density gradients throughout the flow. This result is clearly visible in Figures 18a and 18b. As the Mach number increases, so does the compressibility of the flow, thus leading to a nearly 60% higher entropy generation. Moreover, as it would be expected, a finer mesh leads to more accurate results, as the flow dynamics can be captured at a smaller scale. Finally, it can be appreciated how the entropy generation is much more abrupt for the transonic case, given the existence of a shock.

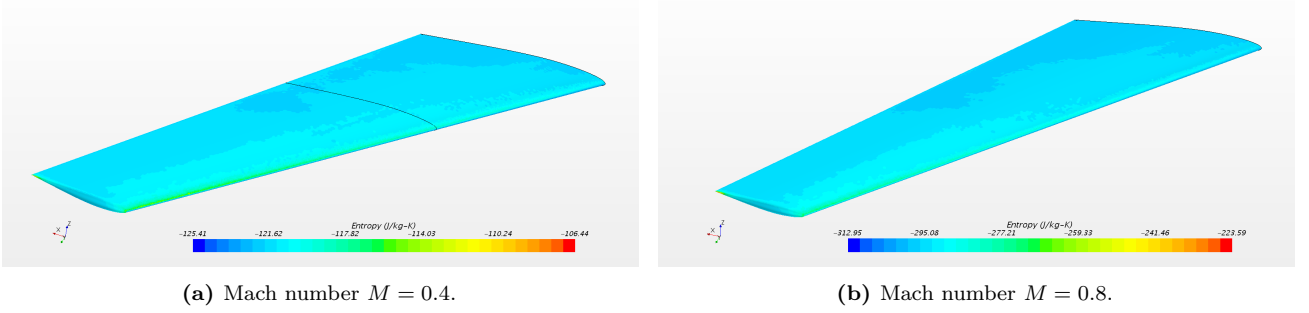


Figure 18: Entropy variation for the inviscid simulation with a fine mesh at various mach numbers.

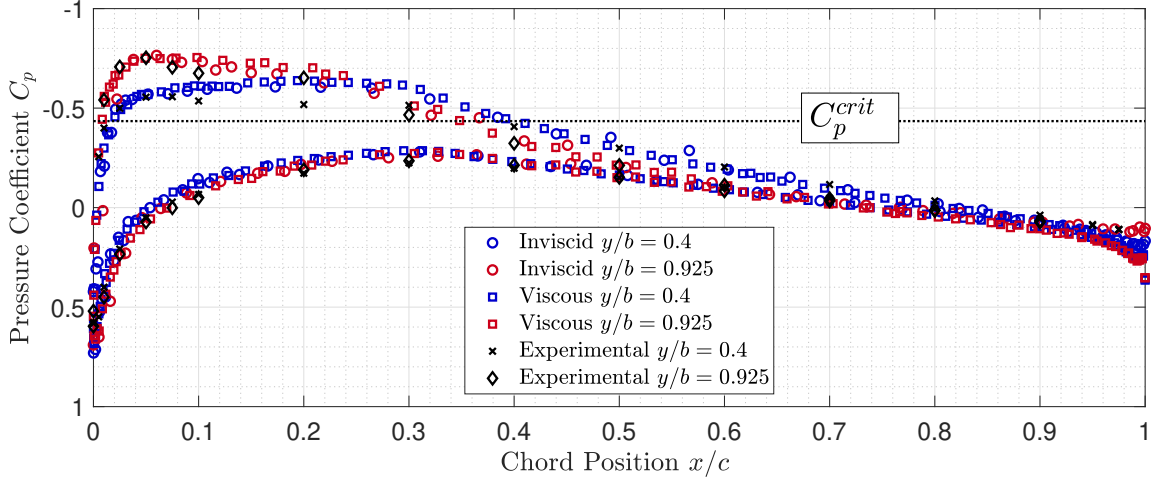


Figure 19: Pressure coefficient distributions for a fine mesh at a Mach number of $M = 0.8$.

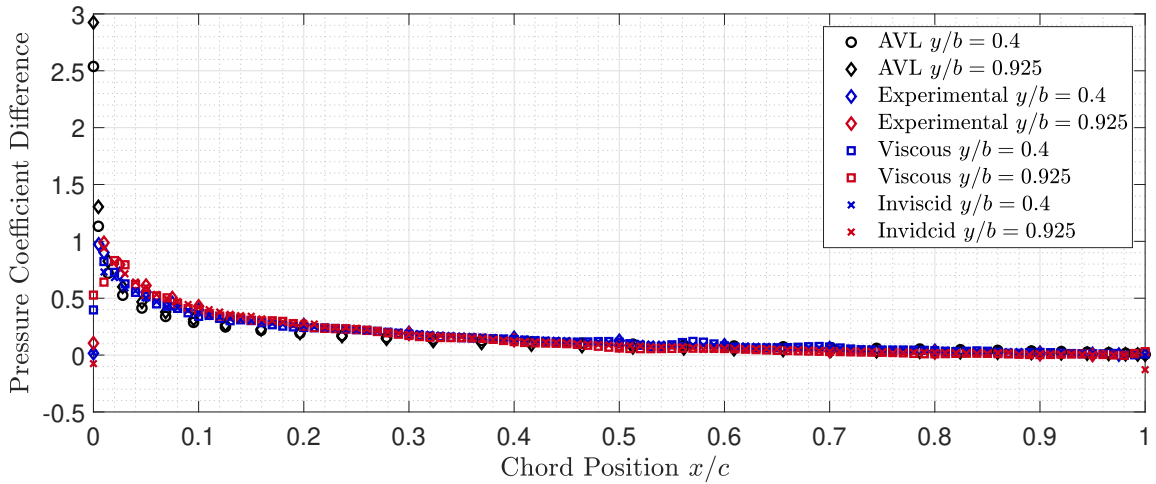


Figure 20: Pressure coefficient differences distributions at a Mach number of $M = 0.8$.